International Journal of Heat and Mass Transfer 67 (2013) 131–146

Contents lists available at ScienceDirect

International Journal of Heat and Mass Transfer

journal homepage: www.elsevier.com/locate/ijhmt

Investigation of localized dryout versus CHF in saturated flow boiling

Christopher Konishi [a], Issam Mudawar [a,*], Mohammad M. Hasan [b]

[a] Boiling and Two-Phase Flow Laboratory (BTPFL), School of Mechanical Engineering, Purdue University, 585 Purdue Mall, West Lafayette, IN 47907, USA
[b] NASA Glenn Research Center, 21000 Brookpark Road, Cleveland, OH 44135, USA

ARTICLE INFO

Article history:
Received 10 April 2013
Received in revised form 24 July 2013
Accepted 25 July 2013
Available online 29 August 2013

Keywords:
Flow boiling
Critical heat flux
Flow orientation

ABSTRACT

Determining flow boiling critical heat flux (CHF) using mechanistic models or empirical correlations requires careful validation with the aid of reliable databases. But, while many new databases are being made available in the literature, the methods used to detect CHF vary greatly, producing different CHF estimates for the same fluid and operating conditions. The variations in detection method are the result of both heated wall design and criteria used to terminate an experiment in response to wall temperature excursions. This study investigates the interfacial phenomena preceding the occurrence of CHF for flow boiling with a finite inlet vapor void. Experiments are conducted with FC-72 in a rectangular channel that is heated along one side. Temporal records of the heated wall temperatures are used to track the complex transient response of the heated wall, and identify differences between temperature excursions associated with momentary localized dryout and those with true CHF. It is shown that the flow enters the channel fully separated, with a liquid layer sheathing all four channel walls surrounding a central vapor core. At high heat fluxes, a wavy vapor layer begins to form beneath the liquid layer adjacent to the heated wall, and cooling is provided mostly through wetting fronts associated with the wave troughs in accordance with the Interfacial Lift-off Model. However, depending on mass velocity, inlet quality and flow orientation, conditions may arise that cause breakup of the heated wall liquid layer into ligaments that are entrained in the vapor core. This phenomenon causes localized dryout and wall temperature excursions at heat fluxes well below CHF, but the wall is able to recover from these excursions by a combination of reattachment of ligaments with the heated wall and lateral heat conduction within the wall itself. Recommendations are made concerning construction of the heated wall and CHF detection in pursuit of reliable CHF data.

1. Introduction

1.1. Implementation of two-phase thermal management in future space missions

As space missions increase in scope, size and power requirements, there is a keen interest among space vehicle developers to increase the efficiency of power utilization by reducing system weight. One system where weight reduction is receiving considerable attention is the Thermal Control System (TCS), which is responsible for controlling the temperature and humidity of the operating environment [1,2].

The TCS is comprised of components that extract heat from a number of sources, including avionics and cabin, and transport the heat to a radiator, where the heat is rejected to deep space. Most previous large space vehicles, including NASA's space shuttles, relied on a single-phase liquid TCS for thermal management. To reduce weight, the TCS in future space systems will be converted to two-phase operation to capitalize on the merits of latent heat of the working fluid rather than sensible heat alone [1,2]. The weight reduction is a direct result of the orders of magnitude enhancement in evaporation and condensation heat transfer coefficients compared to heat transfer coefficients realized with single-phase liquid operation.

Several configurations are possible for extracting heat by evaporation, including pool boiling [3,4], channel flow boiling [5–7], jet [8–11] and spray [12,13], and the use of both enhanced surfaces [14–16] and hybrid cooling schemes that combine the merits of two or more configurations [17,18]. However, implementing those two-phase configurations in reduced gravity is by no means a straightforward endeavor. One of the most complicating factors is the uncertainty concerning the influence of buoyancy on flow boiling and, especially, critical heat flux (CHF) at different gravity levels, and the desire to reduce pumping power and maintain high reliability. These concerns point to channel flow boiling as the method of choice for future space systems.

* Corresponding author. Tel.: +1 765 494 5705; fax: +1 765 494 0539.
E-mail address: mudawar@ecn.purdue.edu (I. Mudawar).
URL: https://engineering.purdue.edu/BTPFL (I. Mudawar).

0017-9310/$ - see front matter © 2013 Elsevier Ltd. All rights reserved.
http://dx.doi.org/10.1016/j.ijheatmasstransfer.2013.07.082

Nomenclature

A	cross-sectional area of flow channel
A_w	area of wetting front
b	ratio of wetting front length to wavelength
c	wave speed
$C_{f,i}$	interfacial friction coefficient
c_p	specific heat at constant pressure
D	diameter
f	friction factor
G	mass velocity
g_e	Earth gravitational acceleration
H	height of flow channel; layer thickness
h	heat transfer coefficient
h_{fg}	latent heat of vaporization
k	wave number; thermal conductivity
L	length
$\dot{m}$	mass flow rate
$\dot{m}'_{fg}$	liquid evaporation rate between heated wall liquid and vapor layers
p	pressure
P_i	interfacial perimeter
P_w	perimeter in contact with channel walls
q''	wall heat flux
q''_m	critical heat flux
Re	Reynolds number
T	temperature
t	time
U	mean axial velocity
u_i	interfacial velocity
W	width of flow channel
x_e	thermodynamic equilibrium quality
x_f	liquid mass flow fraction
y	coordinate normal to heated wall
z	axial distance
z_0	axial location where vapor layer velocity just exceeds liquid layer velocity
z^*	axial location for determining vapor layer thickness and critical wavelength in Interfacial Lift-off Model

Greek symbols

α	vapor (area-based) void fraction
δ	vapor layer thickness; wall thickness
ε_f	liquid area fraction
η	interfacial perturbation
θ	flow orientation angle
λ	wavelength
λ_c	critical wavelength
μ	dynamic viscosity
Π	dimensionless group
ρ	density
ρ''	modified density
σ	surface tension
τ_i	interfacial shear stress
τ_w	wall shear stress

Subscripts

1	insulated wall liquid layer
2	middle vapor core
3	heated wall liquid layer
4	heated wall wavy vapor layer
asy	asymptotic wall thickness
c	critical
f	saturated liquid
g	saturated vapor
h	heated wall
i	interface
in	inlet to heated portion of flow channel
k	phase k, $k = g$ or f
n	normal to heated wall
sat	saturation
sub	subcooling
w	wall; wetting front

1.2. Limitations of critical heat flux (CHF) correlations

CHF is arguably the most important design and safety parameter for heat-flux-controlled two-phase flow systems. Depending on the working fluid and operating conditions, CHF occurrence can trigger physical meltdown, burnout, or another form of permanent physical damage to the heat-dissipating surface. But, while the importance of this phenomenon is clearly understood, there is considerable confusion about its trigger mechanism, experimental detection and measurement, and prediction.

A vast number of studies conducted mostly since the 1940s aimed at exploring these very issues. Because of the complexity of hydrodynamic and thermal characteristics of flow boiling, the primary contribution from most studies has been the accumulation of CHF data and development of empirical correlations applicable to specific fluids, flow geometries and operating conditions. Despite the great value of these contributions, two-phase system designers are often confronted with great difficulty predicting CHF with acceptable accuracy. As explained by Mudawar [19], the primary reason behind this difficulty can be explained as follows for the special case of flow boiling in tubes. A typical CHF correlation for tube flows takes the form

$$\frac{q''_m}{Gh_{fg}} = f\left(\frac{\rho_f}{\rho_g}, \frac{G^2 L}{\sigma\rho_f}, \frac{c_{p,f}\Delta T_{sub}}{h_{fg}}, \frac{L}{D}, \frac{G}{\rho_f\sqrt{g_e D}}, \cdots\right)$$

$$= f(\Pi_1, \Pi_2, \Pi_3, \Pi_4, \Pi_5, \ldots) \quad \begin{cases} \Pi_{1,min}, < \Pi_1 < \Pi_{1,max}, \\ \Pi_{2,min} < \Pi_2 < \Pi_{2,max}, \\ \Pi_{3,min} < \Pi_3 < \Pi_{3,max}, \\ \Pi_{4,min} < \Pi_4 < \Pi_{4,max}, \\ \Pi_{5,min} < \Pi_5 < \Pi_{5,max}, \\ \quad . \\ \quad . \end{cases} \tag{1}$$

Unlike single-phase heat transfer coefficient correlations that generally consist of one dependent parameter (Nusselt number) as a function of only two independent parameters (Reynolds and Prandtl numbers), CHF correlations are far more complex. Eq. (1) shows (i) CHF correlations consist of a dimensionless group that is a function of numerous independent dimensionless groups, and (ii) each independent group is valid over a finite range. Furthermore, because of the high cost of conducting two-phase experiments compared to their single-phase counterparts, CHF data from individual sources are comparatively sparse, and coverages of the individual independent parameters quite limited. Therefore, when a CHF database is

consolidated from different sources in pursuit of CHF correlation, the resulting database is restricted to narrow ranges of many parameters, and the CHF correlation is valid over a very small region of the multidimensional space representing all independent parameters. Because of this limitation, thermal system designers are often forced to employ correlations beyond the parameter ranges for which these correlations are recommended. This is undoubtedly one of the primary reasons for inaccurate CHF predictions.

The alternative to empirical correlations is to develop theoretical models based on dominant CHF trigger mechanisms. The saturated pool boiling CHF model by Zuber et al. [20] is arguably the best example of a successful theoretical formulation for boiling applications. Unfortunately, CHF in flow boiling is significantly more complicated and exhibits different forms depending on working fluid and operating conditions.

1.3. CHF trigger mechanisms and models

Despite the confusion concerning the precise mechanism for CHF, researchers concur that, for heat-flux-controlled systems, CHF is associated with a sharp rise in wall temperature and appreciable reduction in local heat transfer coefficient resulting from inadequate liquid access to the wall. Two different terms that are commonly used to describe specific types of CHF are *Dryout* and *Departure from Nucleate Boiling* (DNB) [21]. Dryout occurs in high quality flows exhibiting an annular flow boiling regime. Here, the heat supplied to the fluid causes gradual thinning of the annular liquid film, and the term 'dryout' is used to describe complete evaporation of the liquid film as the cause for CHF. DNB is more prevalent with subcooled inlet conditions and higher mass velocities, and corresponds to loss of liquid access to the heated wall despite the existence of adequate liquid elsewhere in the tube's cross section. In general, dryout represents a milder form of CHF and is encountered at lower heat fluxes. DNB, on the other hand, corresponds to higher wall heat fluxes and results in faster wall temperature excursion and therefore higher potential for physical damage to the heated wall.

Four different CHF models have been proposed for flow boiling in tubes: *Boundary Layer Separation, Bubble Crowding, Sublayer Dryout,* and *Interfacial Lift-off*, which are illustrated schematically in Fig. 1. The Boundary Layer Separation Model [22,23] is based on analogy between wall fluid injection – transpiration – into a single-phase boundary layer and vapor effusion at the wall in flow boiling. In the case of single-phase fluid injection, the velocity profile across the boundary layer is diminished, and becomes vanishingly small once the injection velocity reaches a threshold value, which causes the boundary layer to separate from the wall. By analogy, the Boundary layer Separation Model is based on the premise that CHF occurs when the rate of vapor effusion normal to the heated wall reaches a threshold value that causes appreciable reduction in the liquid velocity gradient, and eventual separation of the liquid from the wall. The Bubble Crowding Model [24,25] is based on the observation that liquid access to the wall is greatly impeded by a thick layer of oblong vapor bubbles. Here, CHF is assumed to occur when turbulent fluctuations in the core liquid flow become too weak to support liquid penetration across the thick bubbly wall layer and provide adequate liquid to the wall. The Sublayer Dryout Model [26] is based on the depiction of a wall that is covered with oblong vapor bubbles that trap liquid sublayers with the wall. CHF is postulated to occur when the heat supplied at the wall exceeds the enthalpy of replenishment liquid from the bulk region. The more recent Interfacial Lift-off Model [27–30] is based on the observation that, during vigorous boiling, the vapor coalesces into a fairly continuous wavy vapor layer. Before CHF, bulk liquid is capable of reaching the heated wall and providing adequate cooling in the wave troughs. CHF is postulated to occur when intense vapor production in the troughs causes the wavy interface to be lifted off the wall, extinguishing liquid supply to the wall. The Interfacial lift-off model has been especially effective at predicting CHF for flow boiling in microgravity [31].

1.4. Differences in methods of detecting and measuring flow boiling CHF

Developing reliable CHF correlations and mechanistic models requires systematic methods for CHF detection and measurement. Surprisingly, there is great uncertainty in the heat transfer literature concerning the precise definition of CHF, evidenced by differences in the experimental methods adopted for CHF detection [32,33]. These differences are responsible for drastic differences in measured CHF [34]. Following are the more popular methods for CHF detection: (a) first measureable degradation in flow boiling heat transfer, indicated by a slope change of the upper portion of the nucleate boiling region of the boiling curve [35–37], (b) rise in heated wall temperature above a fixed level dictated by the experimenter [38,39], followed by either manual or automatic power shut-off, (c) appreciable unsteady temperature rise of any portion of the heated wall [40,41], and (d) allowing sufficient,

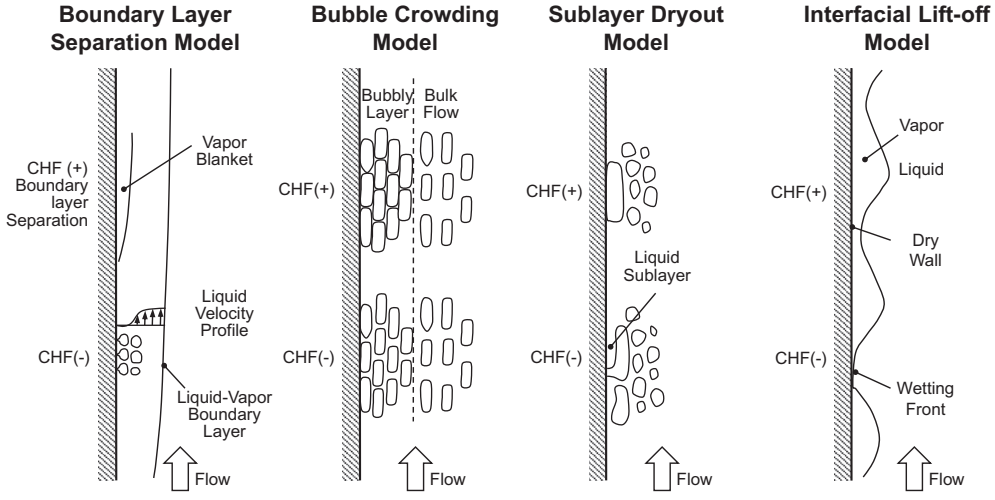

Fig. 1. Trigger mechanisms for flow boiling CHF according to different models.

albeit short period of time for the heated wall to recover from any brief, localized temperature excursion, then increasing heat flux until the wall temperature escalates uncontrollably [42].

Aside from detection method, CHF magnitude can also be greatly influenced by the thickness, δ_h, and thermal properties ($k_h, \rho_h, c_{p,h}$) of the heated wall [43]. For example, some investigators employ extremely thin electrically heating walls (*e.g.,* semi-transparent gold film sputtered on a quartz wall) for CHF measurement [44–46]). The concern with this type of heated wall construction is that it may be too thin to permit momentarily dry portions of the wall to be cooled by lateral conduction to other adequately cooled portions. Theoretically speaking, very thin walls may falsely detect CHF even in the low heat flux region of nucleate boiling once dryout occurs, say, beneath a single growing bubble. Very thin heating walls are both unrepresentative of practical surfaces and known to yield CHF values considerably smaller than those of practical walls. To achieve reliable CHF measurement, a sufficient heated wall thickness is required. Fig. 2 illustrates this phenomenon by the variation of CHF for FC-72 with copper wall thickness [31]. It shows very thin walls yield unusually small CHF values, and CHF increasing with increasing thickness up to 0.4 mm, above which it assumes a constant asymptotic value that is representative of practical walls. Hence, it is important to employ a wall thickness for CHF measurement that falls within the asymptotic range.

1.5. Objectives of study

The present study is an investigation into interfacial phenomena preceding the occurrence of CHF for flow boiling with finite vapor void at the inlet. Experiments are conducted by boiling FC-72 along a rectangular channel fitted with a heated wall along one side. The key variables for the study are mass velocity, inlet quality and flow orientation relative to Earth's gravity. Temporal records of the heated wall temperatures are used to identify differences between temperature excursions associated with momentary localized dryout and true CHF.

2. Experimental methods

2.1. Flow boiling module and flow loop

The flow boiling module used in this study is configured to enable both detailed heat transfer measurements and video analysis of the flow. The module consists of two transparent polycarbonate plastic (Lexan) plates that are bolted together, with a 5.0-mm high by 2.5-mm wide flow channel machined into the underside of the top plate as illustrated in Fig. 3(a). The downstream portion of the bottom plate is hollowed out to accommodate a heating wall consisting of 0.56-mm thick and 101.6-mm long copper plate that is heated by a series of thick film resistors. The flow channel is comprised of an adiabatic entry length 106 times the hydraulic diameter, followed by the section containing the heated wall, and a downstream adiabatic section. The flow boiling module in mounted on a 0–360° swivel to allow testing at any flow orientation relative to Earth's gravity.

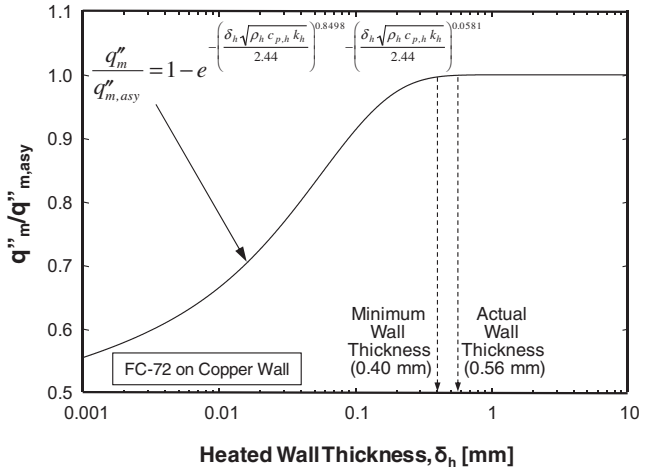

Fig. 2. Effect of wall thickness on CHF, and determination of wall thickness to attain CHF values that are representative of metallic walls of practical interest. Adapted from Zhang et al. [31].

2.2. Heated wall construction

Originally designed for parabolic flight microgravity experiments [31], the heated wall consists of six 4.0-mm wide by 16.1-mm long, thick-film resistors that are soldered to the underside of the copper plate, Fig. 3(b), and connected in parallel to a single 115-volt ac variac. The heated wall temperature is measured by five type-K thermocouples that are inserted into small holes in the copper plate between the resistors at the axial locations indicated in Fig. 3(c).

One of the primary challenges in selecting an optimum thickness for the copper plate is to simultaneously satisfy two crucial criteria. The first is to minimize wall thickness in pursuit of fast temperature response to achieve steady state temperatures following a small power increment within a typical parabola (~17–23 s) [31]. The second is to ensure that the measured CHF is representative of practical walls. As shown in Fig. 2, the minimum thickness that precludes CHF dependence on wall thickness for boiling of FC-72 on copper is 0.40 mm, which is why a thickness of 0.56 mm is used [31].

2.3. Two-phase flow loop

A two-phase flow loop is constructed to supply FC-72 to the flow boiling module at the desired flow rate, pressure and quality. As shown in Fig. 3(d), the FC-72 liquid resides in a reservoir, which also serves as a deaeration chamber, from which the liquid is pumped into the flow boiling module after passing through a filter, turbine flow meter, and two in-line electric pre-heaters. The two-phase mixture exiting the flow boiling module passes through an air-cooled heat exchanger to return to liquid state. A nitrogen-filled accumulator is included to provide a reference pressure point for the loop.

2.4. Flow visualization techniques

Analysis of interfacial features along the flow channel is achieved with a high-speed Photron Fastcam Ultima APX video camera with a shutter speed of 1/20,000 s, which is fitted with a high magnification Nikon Micro-Nikkor 105 mm f/8D autofocus lens. Video capture is achieved at a frame rate of 4000 fps, with the heated channel backlit using a high intensity light source that is diffused across a Mylar sheet. As shown in Fig. 4(a) and (b), the camera is aimed normal to the side of the flow channel, and the imaging is repeated in 20-mm long inlet, middle, and outlet portions of the heated wall.

2.5. Operating conditions and measurement accuracy

The test facility provides broad coverage of mass velocity, G/ρ_f = 0.126–1.130 m/s, and channel inlet quality, $x_{e,in}$ = 0.01–0.19, at eight orientations, Fig. 4(c), with the pressure at the outlet of the heated wall maintained at 103 kPa (15 psia).

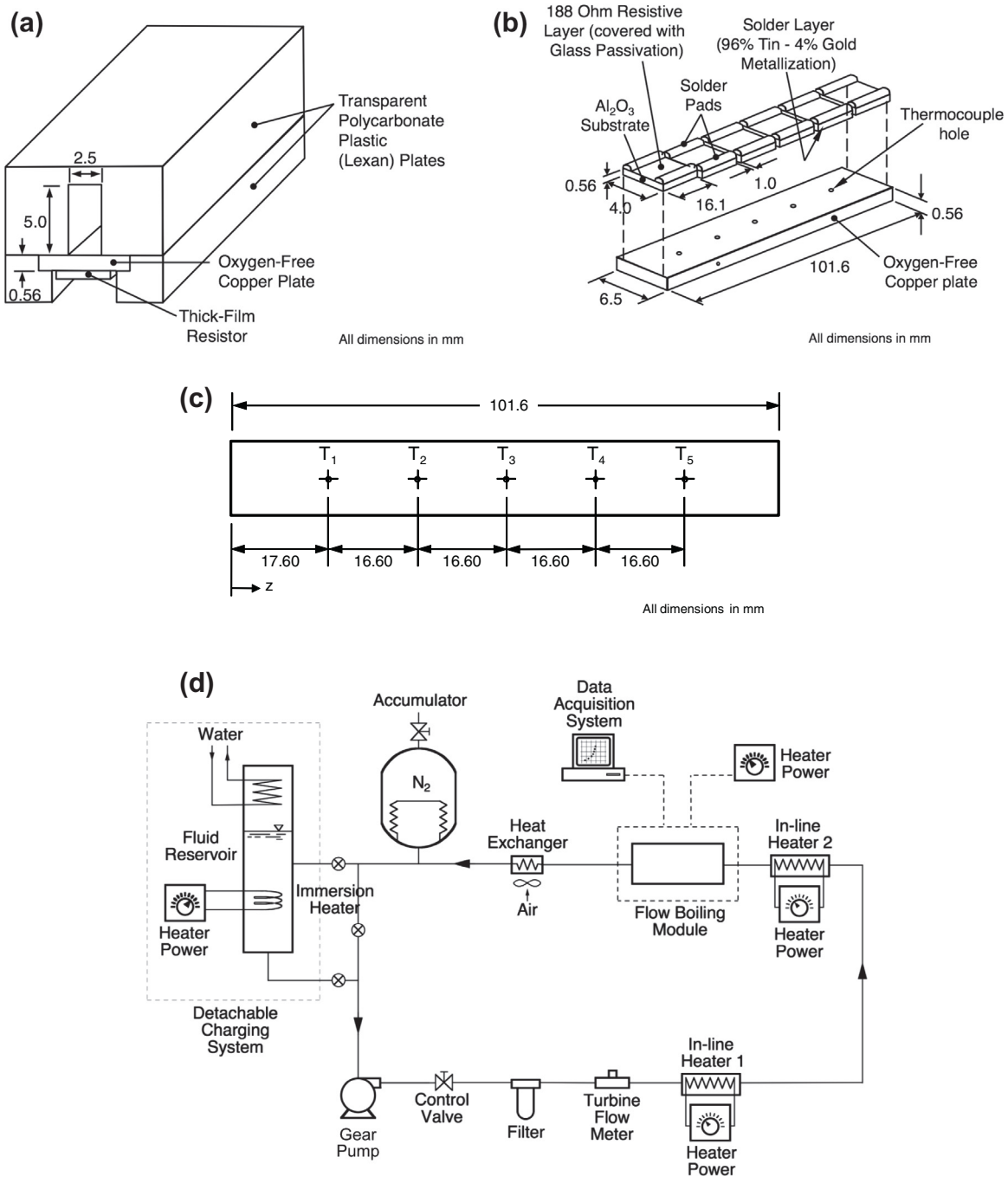

Fig. 3. (a) Construction of flow boiling module. (b) Construction of heated wall. (c) Axial locations of heated wall thermocouples. (d) Schematic diagram of flow loop.

Fluid temperature and pressure are measured both upstream and downstream of the heated wall, as well as at various locations in the loop. The accuracies of the pressure transducer and temperature measurements are estimated at 0.01% and 0.3 °C, respectively.

The wall thermocouples are calibrated by placing the instrumented heated wall in ice water and using the data acquisition system to increase or decrease the measurements of individual thermocouples to read zero temperature. The heated wall is then placed in a constant temperature oven. The thermocouple signals are calibrated at several oven temperature settings up to and including 100 °C. At each setting, individual signals are adjusted by the data acquisition system to read a temperature equal to the mean of the heated wall thermocouple signals. The heated wall thermocouples are therefore calibrated in this manner over the temperature range 0–100 °C.

A systematic method is adopted for determining heat loss from the heated wall. For single-phase flow, the heat loss can be easily determined by comparing the fluid's sensible heat rise to the electrical power input. But this method cannot be applied in two-phase situations. The method used to determine the heat loss involves an iterative calculation scheme. Initially, zero heat loss is assumed and the convective heat transfer coefficients are calculated at the axial locations of the thermocouples. A finite element model is constructed for the test module, which accounts for heat that is lost through the channel walls and external natural convection. Boundary conditions for the channel in the finite element model are determined by applying the heat transfer coefficient variation from

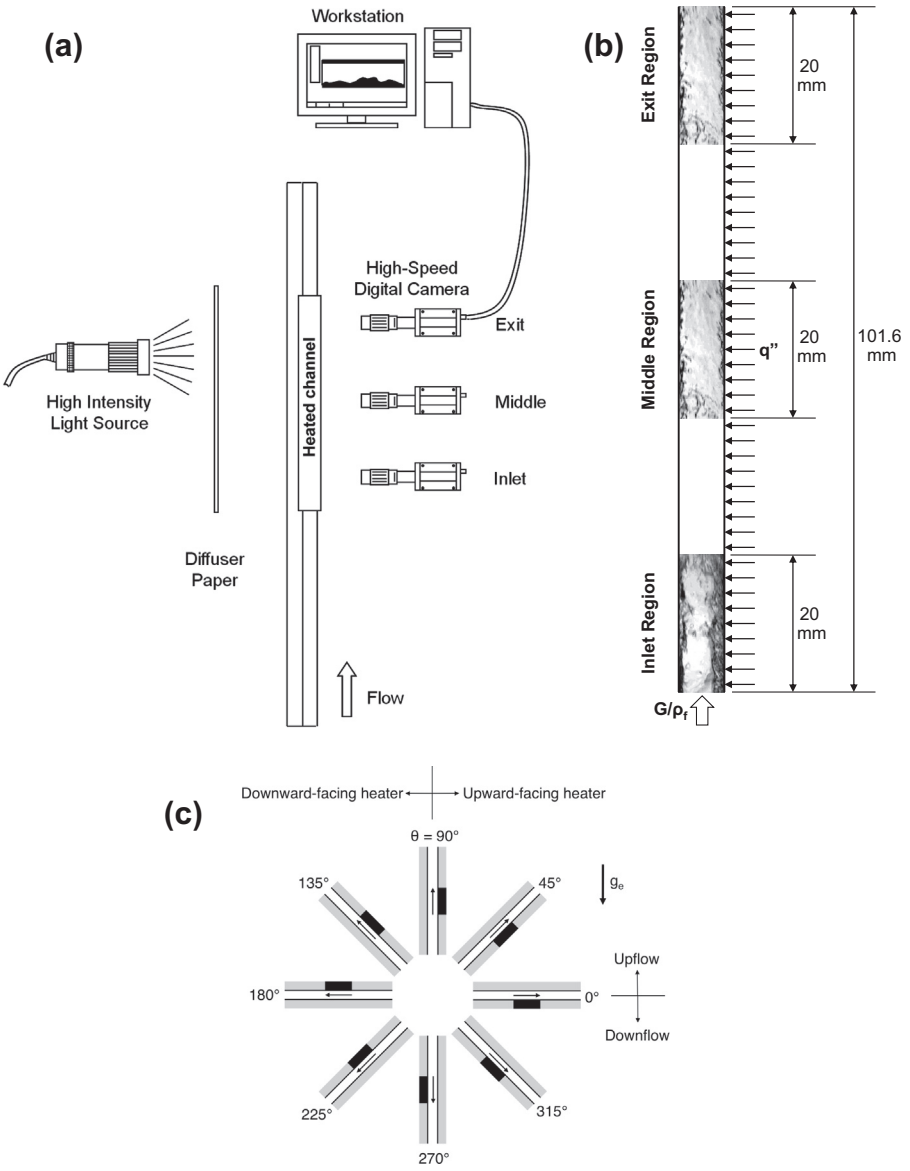

Fig. 4. (a) Flow visualization setup. (b) Axial spans of video capture regions of the heated wall. (c) Channel flow orientations relative to Earth's gravity; heated wall is identified for each orientation by a black strip.

the first iteration, and heat loss is estimated using the finite element model. In a second iteration, the value of wall heat flux is adjusted by deducting heat loss from the total electrical power input. New values of the convective heat transfer coefficients are determined, and these updated values are used in the model to yield an updated estimate for heat loss. Further iteration is attempted until the heat transfer coefficient values converge. This technique is used to determine the uncertainty in heat flux measurement due to heat loss alone. Accounting for error propagation due to thermocouples, pressure transducers, turbine flow meter, and power meter, the maximum uncertainty in the heat transfer measurements is 0.2% of the electrical power input.

3. Formulation of Interfacial Lift-off CHF Model for subcooled and saturated flow boiling

3.1. Basic formulation of model for subcooled inlet conditions

Originally proposed by Galloway and Mudawar [27,28], the Interfacial Lift-off Model is based on extensive video analysis of interfacial features associated with flow boiling along a heated wall at conditions just before and during CHF. The model was proven effective at predicting CHF with remarkable accuracy for different channel sizes and operating conditions [29,30,47,48]. All these earlier studies involved one sided heating in a rectangular channel with the fluid supplied in pure liquid state.

The foundation of the Interfacial Lift-off Model is the observation that, as CHF is approached, vapor bubbles coalesce first into larger oblong vapor bubbles and subsequently a fairly continuous wavy vapor layer. Just before CHF, the wall is adequately cooled by liquid access to the heated wall through the wave troughs, termed wetting fronts. A further increase in wall heat flux causes intense vapor effusion in the wetting fronts to separate the wavy interface from the wall, extinguishing the liquid access.

The Interfacial Lift-off Model uses hydrodynamic instability to describe the wavy interface between a liquid layer of mean velocity U_f and mean thickness H_f, and a vapor layer of mean velocity U_g and mean thickness H_g as shown in Fig. 5(a). Formation of wetting fronts requires that the interfacial wavelength exceed the critical wavelength, λ_c, which is given by

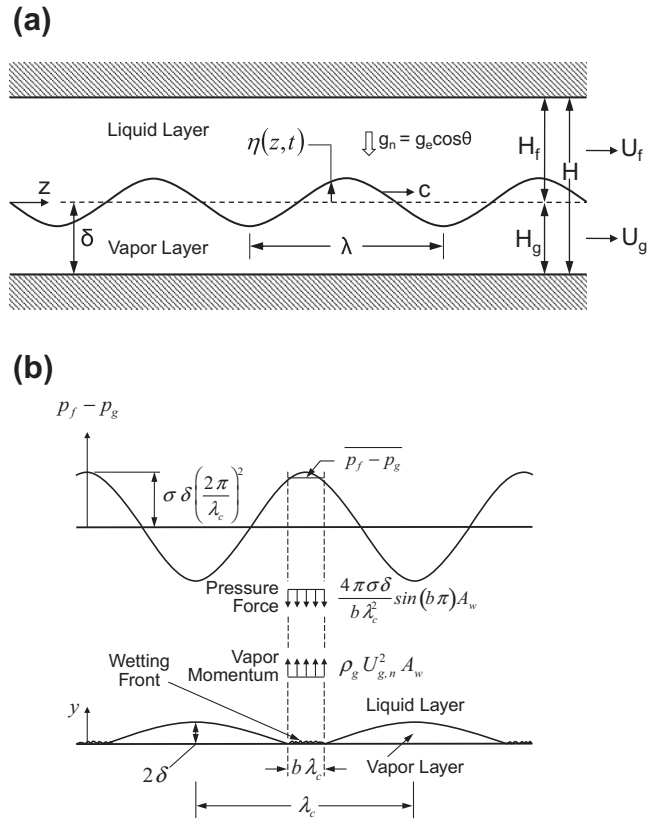

Fig. 5. (a) Wavy interface between liquid and vapor layers. (b) Interfacial lift-off of wetting front at CHF.

$$k_c = \frac{2\pi}{\lambda_c} = \frac{\rho_f'' \rho_g'' (U_g - U_f)^2}{2\sigma\left(\rho_f'' + \rho_g''\right)} + \sqrt{\left[\frac{\rho_{f3}'' \rho_{g4}'' (U_g - U_f)^2}{2\sigma\left(\rho_f'' + \rho_g''\right)}\right]^2 + \frac{(\rho_f - \rho_g) g_e \cos\theta}{\sigma}}, \quad (2)$$

where $\rho_f'' = \rho_f coth(kH_f)$ and $\rho_g'' = \rho_g coth(kH_g)$ are 'modified density' terms, and $g_e\cos\theta = g_n$, the component of gravity perpendicular to the heated wall. Notice that large velocity differences tend to destabilize the interface while surface tension helps preserve interfacial stability. Depending on the orientation relative to gravity, body force can be stabilizing or destabilizing.

The second part of the Interfacial Lift-off Model concerns separation of wetting fronts from the wall, which constitutes the *trigger* mechanism for CHF. Notice that curvature of the liquid–vapor interface generates a pressure force that promotes the interfacial contact with the heated wall responsible for preserving the liquid replenishment. CHF is postulated to occur when the normal momentum of vapor generated in the wetting front just exceeds the pressure force. For an assumed interfacial wave shape of the form $\eta(z,t) = \eta_o e^{ik(z-ct)}$, the pressure difference perpendicular to the wall is expressed as

$$p_f - p_g = -\left[\rho_f''(c - U_f)^2 + \rho_g''(c - U_g)^2 + (\rho_f - \rho_g)\frac{g_n}{k}\right] k\eta_0 e^{ik(z-ct)}. \quad (3)$$

Assuming the wetting front occupies a fixed fraction b of the critical wavelength, the average pressure force for a wetting front is determined by averaging the pressure difference over $b\lambda_c$,

$$\overline{p_f - p_g} = \frac{4\pi\sigma\delta}{b\lambda^2}\sin(b\pi), \quad (4)$$

where δ represents the mean vapor layer thickness. Illustrated in Fig. 5(b), the normal vapor momentum $\rho_g U_{g,n}^2$ emanating from a wetting front of length $b\lambda$ is opposed by the pressure force.

Using extensive video records and statistical averaging techniques, Sturgis and Mudawar [29,30] showed that $b = 0.2$ over a broad range of flow conditions. They detected a continuous wetting region of length z^*, defined as $z^* = z_o + \lambda_c(z^*)$, where z_o is the distance from the leading edge of the heated wall to the location where U_g surpasses U_f. The wavy interface is therefore generated at z^* and propagates downstream.

Considering flow boiling with a subcooled inlet, the heat concentrated in a wetting front is consumed by vaporizing liquid, $q_w'' A_w = (c_{pf}\Delta T_{sub,in} + h_{fg})\rho_g U_{g,n} A_w$, where A_w is the wetting front area. The local heat flux required to push the interface away from the wall is determined by equating the vapor momentum, $\rho_g U_{g,n}^2$, to the pressure force obtained from Eq. (4).

$$q_w'' = \rho_g (c_{pf}\Delta T_{sub,in} + h_{fg})\sqrt{\frac{\overline{p_f - p_g}}{\rho_g}} = \rho_g (c_{pf}\Delta T_{sub,in} + h_{fg})\left[\frac{4\pi\sigma}{\rho_g}\frac{\sin(b\pi)}{b}\right]^{1/2}\left.\frac{\delta^{1/2}}{\lambda_c}\right|_{z^*}. \quad (5)$$

The critical heat flux, q_m'', is defined as the average heat flux over the entire heated area, which is related to the wetting front heat flux by the relation $q_m'' = b q_w''$. This gives the following analytical expression for CHF corresponding to subcooled inlet conditions.

$$q_m'' = \rho_g (c_{pf}\Delta T_{sub,in} + h_{fg})\left[\frac{4\ \pi\ \sigma b \sin(b\ \pi)}{\rho_g}\right]^{1/2}\left.\frac{\delta^{1/2}}{\lambda_c}\right|_{z^*}. \quad (6)$$

Notice that δ and λ_c in Eq. (6) are calculated at z^*. These two parameters are determined from a separated flow model that is used to predict $U_f(z)$, $U_g(z)$, and $\delta(z)$.

3.2. Model validation for subcooled inlet conditions with varying body force and microgravity

Zhang et al. [49,50] investigated the influence of body force on flow boiling CHF with subcooled inlet conditions in a rectangular channel with one-sided heating by testing the channel at different orientations relative to Earth's gravity. They identified several mechanisms for CHF that were dictated by a combination of mass velocity, flow orientation, and placement of the heated wall relative to gravity. Complex flow patterns were observed mostly at low mass velocities, downflow and with the heated wall facing downwards. These are all conditions where liquid drag forces are dwarfed by buoyancy. However, CHF for high mass velocities was associated with the same wavy layer behavior illustrated in Fig. 5(a), and triggered by the interfacial lift-off mechanism depicted in Fig. 5(b) regardless of orientation. They demonstrated the validity of the Interfacial Lift-off Model for high mass velocities in both interfacial behavior and accuracy.

Later, Zhang et al. [31] performed flow boiling experiments in parabolic flight to simulate microgravity. Absent from these experiments were the complex flow patterns that were prevalent at low mass velocities at different orientations in Earth's gravity. In fact, the wavy vapor layer behavior was encountered in microgravity for all mass velocities, and the Interfacial Lift-off Model showed very good accuracy in predicting the CHF data.

3.3. Model modification for saturated inlet conditions with varying body force

More recently, Kharangate et al. [51,52] performed flow boiling CHF experiments in vertical upflow and horizontal flow, respectively, but with saturated conditions and finite vapor void at the inlet. The large vapor void had a profound influence on two-phase flow behavior leading to CHF. For vertical upflow [51], the fluid was observed to enter the channel fully separated, with a relatively thin liquid layer covering the entire perimeter of the channel surrounding a large central vapor core. Vapor was generated within the portion of the liquid layer in contact with the heated wall and, near CHF, the vapor coalesced into a wavy vapor layer that began to separate from the heated wall. By incorporating modifications to account for the inlet void and multiple flow layers, the Interfacial Lift-off Model was shown equally effective at predicting CHF for saturated inlet conditions.

Konishi et al. [53,54] extended the work of Kharangate et al. by investigating flow boiling CHF with a finite inlet void at all flow orientations depicted in Fig. 4(c). Similar to the findings of Zhang et al. [49,50], low mass velocities were observed to yield complex interfacial behavior at CHF. However, moderate mass velocities caused appreciable diminution in the influence of orientation on CHF, evidenced by similar flow patterns and CHF trigger mechanism regardless of orientation. The modified Interfacial Lift-off Model was shown to predict the influence of orientation on CHF for moderate to high mass velocities and with good accuracy.

Modifying the Interfacial Lift-off Model for the influence of saturated inlet conditions with a finite vapor void requires the determination of mean velocities for liquid and vapor layers adjacent to the heated wall, as well as the thickness of the vapor core layer. Following [53], the flow at CHF- at moderate and high mass velocities enters the channel fully separated, with a liquid film covering all four channel walls surrounding a central vapor core. Shown in Fig. 6(a) are two different cross-sections of the flow, one for the upstream adiabatic region and the other the heated region. Upon entering the heated region, the liquid layer in contact with the heated wall begins to evaporate, initiating a wavy-vapor layer. Fig. 6(a) identifies the individual layers of the flow along the heated wall: liquid layer 1 along the three adiabatic walls of the channel, central vapor layer 2, liquid layer 3 adjacent to, but separated from the heated wall, and vapor layer 4 at the heated wall beneath liquid layer 3. Two separate sets of separated flow equations are used, one for the upstream adiabatic region and the other for the heated downstream region.

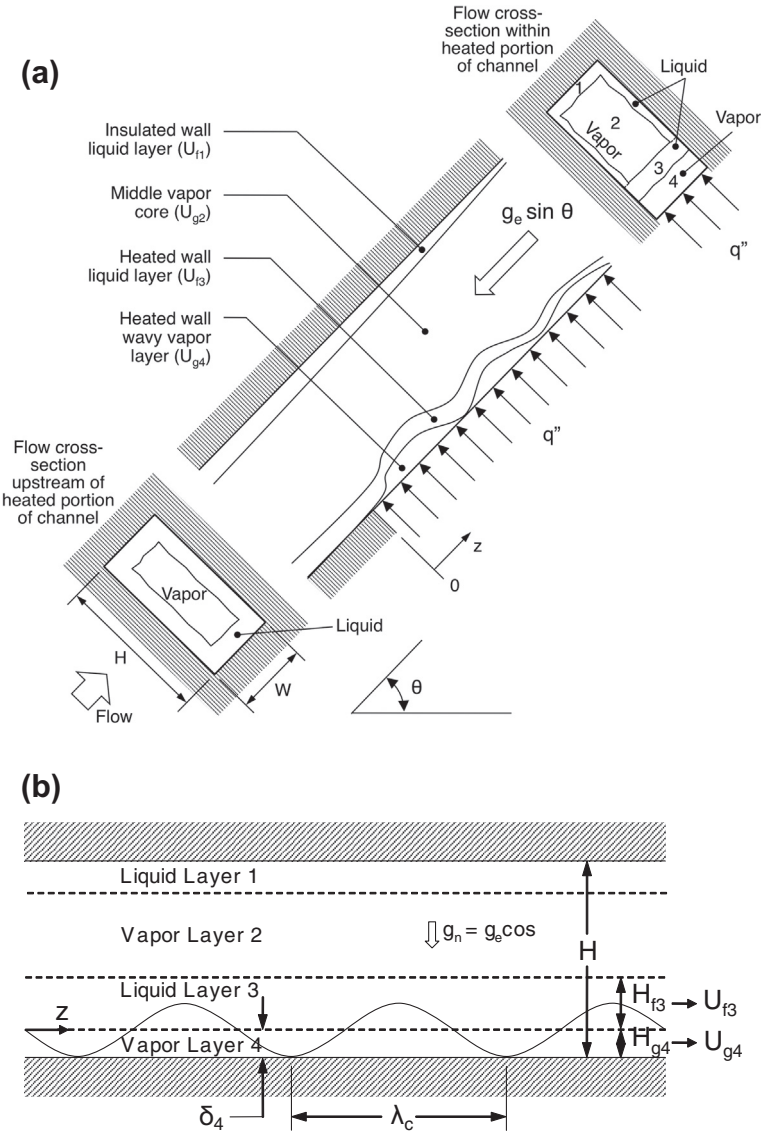

Fig. 6. (a) Schematic of separated layers at CHF- for saturated inlet conditions. (b) Idealized wavy vapor layer formation along heated wall at CHF-.

Table 1
Summary of relations used in conjunction with four-layer separated flow model.[53].

1. Upstream adiabatic region:
Quality relations for individual layers:

$$x_{f1,in}=\frac{W+2H}{2W+2H}\,(1-x_{e,in}),\quad x_{f3,in}=\frac{W}{2W+2H}\,(1-x_{e,in}),\quad \varepsilon_{f1,in}=\frac{W+2H}{2W+2H}\,(1-\alpha_{in}),\quad \varepsilon_{f3,in}=\frac{W}{2W+2\,H}\,(1-\alpha_{in}).$$

Momentum conservation:

$$G^2\frac{d}{dz}\left[\frac{x_{e,in}^2}{\rho_g\alpha_{in}}\right]=-\alpha_{in}\frac{dp}{dz}\mp\frac{\tau_i P_i}{A}-\rho_g\alpha_{in}g_e\sin\theta,$$

$$G^2\frac{d}{dz}\left[\frac{(1-x_{e,in})^2}{\rho_f(1-\alpha_{in})}\right]=-(1-\alpha_{in})\frac{dp}{dz}-\frac{\tau_{w,f}P_{w,f}}{A}\pm\frac{\tau_i P_i}{A}-\rho_f(1-\alpha_{\mathrm{in}})\,g_e\sin\theta.$$

2. Heated region:
Quality relations for individual layers:

$$x_{f1}=\frac{\rho_f U_{f1}\,\varepsilon_{f1}}{G},\quad x_2=\frac{\rho_g U_{g2}\,\alpha_2}{G}=x_{e,in},\quad x_{f3}=\frac{\rho_f U_{f3}\,(1-\varepsilon_{f1}-\alpha_2-\alpha_4)}{G},\quad x_4=\frac{\rho_g U_{g4}\,\alpha_4}{G}.$$

Momentum conservation:

$$G^2\frac{d}{dz}\left[\frac{x_{f1}^2}{\rho_f\,\varepsilon_{f1}}\right]=-\varepsilon_{f1}\frac{dp}{dz}-\frac{\tau_{wf1}\,P_{w,f1}}{A}\pm\frac{\tau_{i12}\,P_{i12}}{A}\mp\frac{\tau_{i13}\,P_{i13}}{A}-\rho_f\,\varepsilon_{f1}\,g_e\sin\theta,$$

$$G^2\frac{d}{dz}\left[\frac{x_2^2}{\rho_g\,\alpha_2}\right]=-\alpha_2\frac{dp}{dz}\mp\frac{\tau_{i12}\,p_{i12}}{A}\mp\frac{\tau_{i23}\,p_{i23}}{A}-\rho_g\alpha_2\,g_e\sin\theta,$$

$$G^2\frac{d}{dz}\left[\frac{x_{f3}^2}{\rho_f\,(1-\varepsilon_{f1}-\alpha_2-\alpha_4)}\right]+\dot{m}_{fg}\,u_{i34}=-(1-\varepsilon_{f1}-\alpha_2-\alpha_4)\,\frac{dp}{dz}-\frac{\tau_{w,f3}\,P_{w,f3}}{A}\pm\frac{\tau_{i13}\,P_{i13}}{A}\pm\frac{\tau_{i23}\,P_{i23}}{A}\pm\frac{\tau_{i34}\,P_{i34}}{A}-\rho_f\,(1-\varepsilon_{f1}-\alpha_2-\alpha_4)g_e\sin\theta$$

$$G^2\frac{d}{dz}\left[\frac{x_4^2}{\rho_g\,\alpha_4}\right]-\dot{m}'_{fg}\,u_{i34}=-\alpha_4\frac{dp}{dz}-\frac{\tau_{w,g4}\,P_{w,g4}}{A}\mp\frac{\tau_{i34}\,P_{i34}}{A}-\rho_g\,\alpha_4\,g_e\sin\theta.$$

Wall shear stress relations:

$$\tau_{w,k,j}=\frac{1}{2}\,\rho_k\,U_{k,j}^2 f_{k,j},$$

$$f_{k,j}=C_1+\frac{C_2}{\mathrm{Re}_{D,k,j}^{1/C_3}}=C_1+\frac{C_2}{\left(\frac{\rho_k U_{k,j}\,D_{k,j}}{\mu_k}\right)^{1/C_3}},$$

where $k=f$ or g, and $j=1$–4. $C_1=0$, $C_2=16$ and $C_3=1$ for laminar flow ($\mathrm{Re}_{D,k,j}\leqslant 2100$), $C_1=0.0054$, $C_2=2.3\times10^{-8}$ and $C_3=-2/3$ for transitional flow ($2100<\mathrm{Re}_{D,k,j}\leqslant 4000$), and $C_1=0.00128$, $C_2=0.1143$ and $C_3=3.2154$ for turbulent flow ($\mathrm{Re}_{D,k,j}>4000$), where $D_{k,j}=4A_{k,j}/P_{k,j}$
Interfacial shear stress relations:

$$\tau_{i12}=\frac{C_{f,i}}{2}\rho_g\,(U_{f1}-U_{g2})^2,\quad \tau_{i23}=\frac{C_{f,i}}{2}\rho_g(U_{g2}-U_{f3})^2,\quad \tau_{i34}=\frac{C_{f,i}}{2}\rho_g(U_{f3}-U_{g4})^2,\quad \tau_{i13}=\frac{C_{f,i}}{2}\rho_g(U_{f1}-U_{f3})^2,$$

where $C_{f,i}=0.5$

Aside from the channel geometry, the key input parameters for the upstream adiabatic region are mass velocity, G, inlet pressure, p_{in}, and inlet quality, $x_{e,in}$. In Table 1, momentum conservation equations for the upstream adiabatic region are written in terms the inlet quality, $x_{e,in}$, inlet void fraction, α_{in}, wall shear stress for the liquid layer, $\tau_{w,f}$, interfacial shear stress, τ_i, channel perimeter, $P_{w,f}$, and perimeter of liquid–vapor interface, P_i. The ± sign of the interfacial shear terms allows for variations in the direction of the shear stress, depending on local velocity differences between the two layers. Neglecting any property variations, mass and

energy conservation result in $dx_{e,in}/dz = 0$ for the adiabatic region. The momentum equations for the upstream region are solved simultaneously using an iterative procedure to determine α_{in}. Relations for the wall and interfacial shear stresses are provided in Table 1.

The inlet mass fractions for liquid layer 1, $x_{f1,in}$, and liquid layer 3, $x_{f3,in}$, are determined from the channel geometry and $x_{e,in}$ as indicated in Table 1. Assuming heat transfer between the vapor core and the liquid layers is negligible, the flow quality of the vapor core is conserved, $x_2 = x_{e,in}$. Equations are included to relate the inlet area fractions for the liquid layer along the adiabatic walls, $\varepsilon_{f1,in}$, and the liquid layer adjacent to the heated wall, $\varepsilon_{f3,in}$, in terms of the channel geometry and inlet void fraction, α_{in}.

Applying mass conservation for the entire heated region results in $d\,\dot{m}/d\,z = 0$, which implies both $\dot{m}$ and G are constant. Neglecting heat transfer between the vapor core and surrounding liquid layers yields constant flow rates for the insulated walls' liquid layer ($x_{f1}\dot{m}$) and central vapor core ($x_2\dot{m}$), which also implies that both x_{f1} and x_2 are constant. The growth of vapor layer (4) along the heated wall is achieved by evaporation of the heated wall liquid layer (3), therefore $x_{f3} = x_{f3,in} - x_4$. The rate of evaporation along the interface between layers 3 and 4 is given by $\dot{m}'_{fg} = GAdx_4/dz$. Energy conservation for the entire cross-sectional area of the channel in the heated region yields $dx/dz = dx_4/dz = q''W/\dot{m}h_{fg}$.

The momentum conservation equations for the heated region in Table 1 are written in terms of, respectively, the wall shear stresses

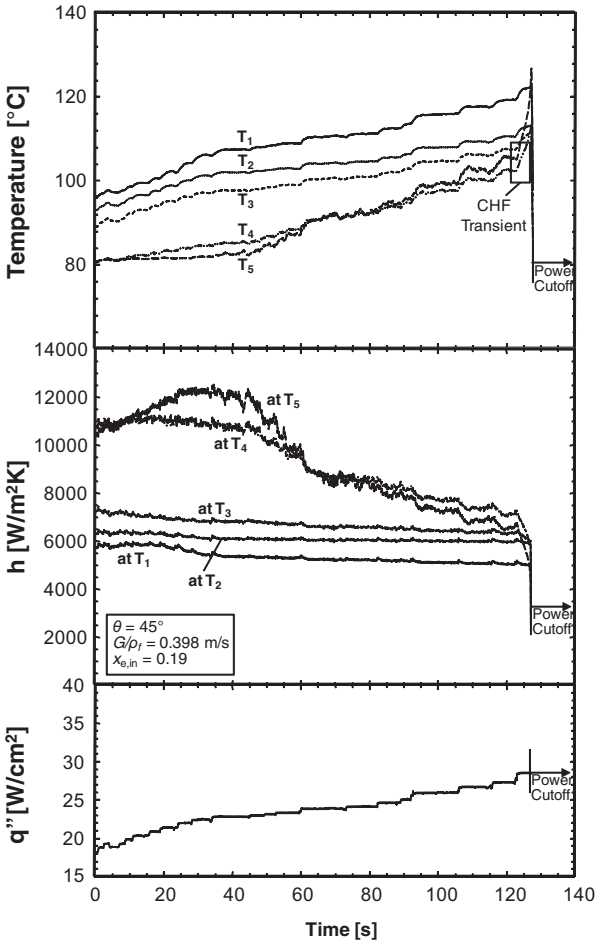

Fig. 7. Temporal records of wall temperatures, heat transfer coefficients and input wall heat flux for $G/\rho_f = 0.398$ m/s, $x_{e,in} = 0.19$ and $\theta = 45°$.

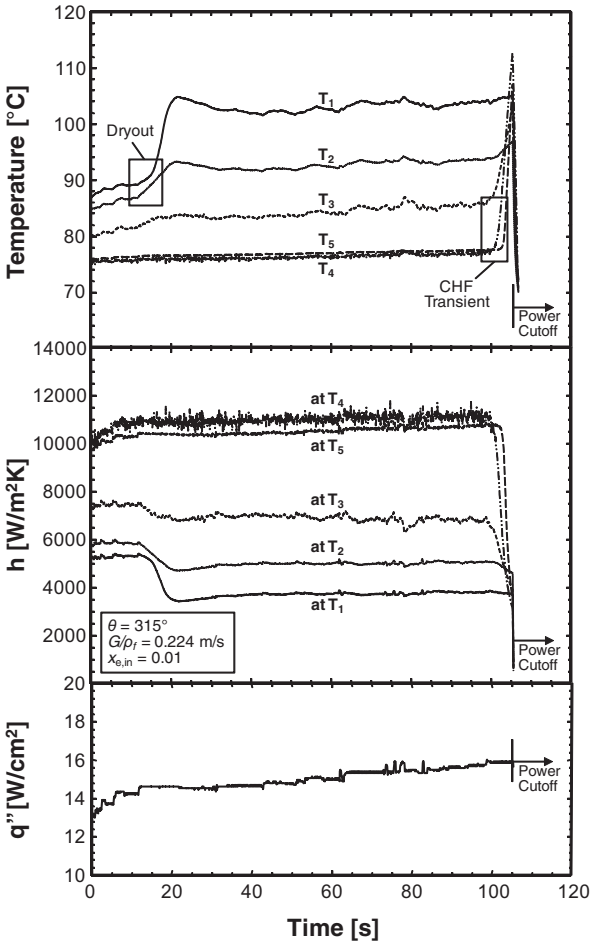

Fig. 8. Temporal records of wall temperatures, heat transfer coefficients and input wall heat flux for $G/\rho_f = 0.224$ m/s, $x_{e,in} = 0.01$ and $\theta = 315°$.

for the insulated walls' liquid layer, heated wall liquid layer, and heated wall vapor layer, $\tau_{w,f1}$, $\tau_{w,f3}$ and $\tau_{w,g4}$, the interfacial shear stresses between the insulated wall liquid layer and vapor core, insulated walls' liquid layer and heated wall liquid layer, vapor core and heated wall liquid layer, and heated wall liquid layer and heated wall vapor layer, τ_{i12}, τ_{i13}, τ_{i23} and τ_{i34}, the wall perimeters of the insulated walls' liquid layer, heated wall liquid layer, and heated wall vapor layer, $P_{w,f1}$, $P_{w,f3}$ and $P_{w,g4}$, and the interfacial perimeters between the insulated walls' liquid layer and vapor core, insulated walls' liquid layer and heated wall liquid layer, vapor core and heated wall liquid layer, and heated wall liquid layer and heated wall vapor layer, P_{i12}, P_{i13}, P_{i23} and P_{i34}.

The separated flow model equations for the heated region are solved using a fourth-order Runge–Kutta numerical scheme using saturated properties based on calculated local pressure. This technique yields detailed axial profiles for local pressure, qualities, area fractions and velocities of the four layers. The main inputs required for the model are mass velocity G, inlet pressure p_{in}, inlet quality $x_{e,in}$, inlet void fraction, α_{in}, and wall heat flux q''.

Fig. 6(b) shows a schematic of the four-layer flow for saturated inlet conditions. The Interfacial Lift-off Model is used here by setting $\Delta T_{sub,in} = 0$ in Eq. (6). The values of mean vapor layer thickness, δ, and critical wavelength, λ_c, are determined at z^* using predictions of the separated flow model for the heated wall liquid layer velocity, U_{f3}, heated wall vapor layer velocity, U_{g4}, and heated wall vapor layer thickness, δ_4.

This modified model will serve as reference for discussion of the complex transient issues leading to CHF for saturated inlet conditions.

4. Transient heat transfer results

A primary goal of the present study is to track the complex thermal transients associated with CHF occurrence for saturated inlet conditions with a finite vapor void. The experiments involved increasing the wall heat flux in small increments and measuring the ensuing temporal variations in wall temperatures. As CHF is approached, localized regions of dryout are observed, but wall temperatures sometimes incurred momentary unsteady excursions that subsided after a finite waiting period. Ultimately, CHF is identified by a fast, uncontrolled rise in any of the wall temperatures.

4.1. Typical transient behavior leading to CHF

Fig. 7 shows a composite plot of temporal records of the heated wall thermocouple signals, heat transfer coefficients at the same axial locations as the thermocouples, and input wall heat flux for $G/\rho_f = 0.398$ m/s, $x_{e,in} = 0.19$ and $\theta = 45°$. These characteristics are representative of CHF occurrence for most operating conditions. The upstream thermocouple is represented by T_1, which is followed by T_2, T_3, T_4 and T_5, with T_5 representing the most downstream thermocouple. The corresponding local heat transfer coefficient at any thermocouple T_i is derived from the simple relation $q'' = h(T_i - T_{sat})$. Contrary to the notion that wall temperatures should increase along the heated wall, Fig. 7 shows wall temperatures are highest at T_1 and for the most part decrease along the flow direction. This behavior can be explained by (i) the vapor core maintaining a fairly constant temperature equal to T_{sat}, and (ii) axial vaporization increasing the velocities of the flow layers, causing a stream-wise increase in the heat transfer coefficient. Notice that CHF is detected downstream by a sharp unsteady rise in the wall temperature starting at T_5 and T_4. The temperature excursions at T_4 and T_5 that precede CHF are in excess of 10 °C over a period of 5 s.

4.2. Dryout anomalies prior to CHF

Pre-CHF anomalies were encountered only with upward-facing heated wall orientations ($\theta = 315°$, 0° and 45°). The dryout typically occurred in the inlet region for low inlet mass velocities of $G/\rho_f \leqslant 0.315$ m/s, and the outlet region for mid-range velocities of $0.542 \geqslant G/\rho_f \geqslant 0.315$ m/s. All other orientations and inlet conditions displayed transient characteristics similar to those shown in Fig. 7.

Fig. 8 shows a composite plot of temporal records for $G/\rho_f = 0.224$ m/s, $x_{e,in} = 0.01$ and $\theta = 315°$. Notice how momentary dryout is first detected at T_1 and, to a lesser extent, T_2 after the wall heat flux is increased by a small increment then held constant. The local dryout excursion at T_1 is about 15 °C in 5 s. Without increasing the heat flux, T_1 begins to level off and decrease slightly before reaching steady state. The wall heat flux is then increased in several small increments, each followed by an adequate waiting period, with all the wall temperatures increasing gradually to new steady state levels with no spikes. Eventually, CHF is detected near the outlet by a sudden uncontrolled temperature rise commencing at T_5 and T_4 with no signs of temperature recovery. These trends point to a very important aspect of CHF detection. Given the large difference in wall heat flux between the time the first dryout is detected at T_1 and the time CHF actually occurs, identifying the temperature spike at T_1 as CHF would undoubtedly lead to a measurable error (~7.5%) in the measured CHF.

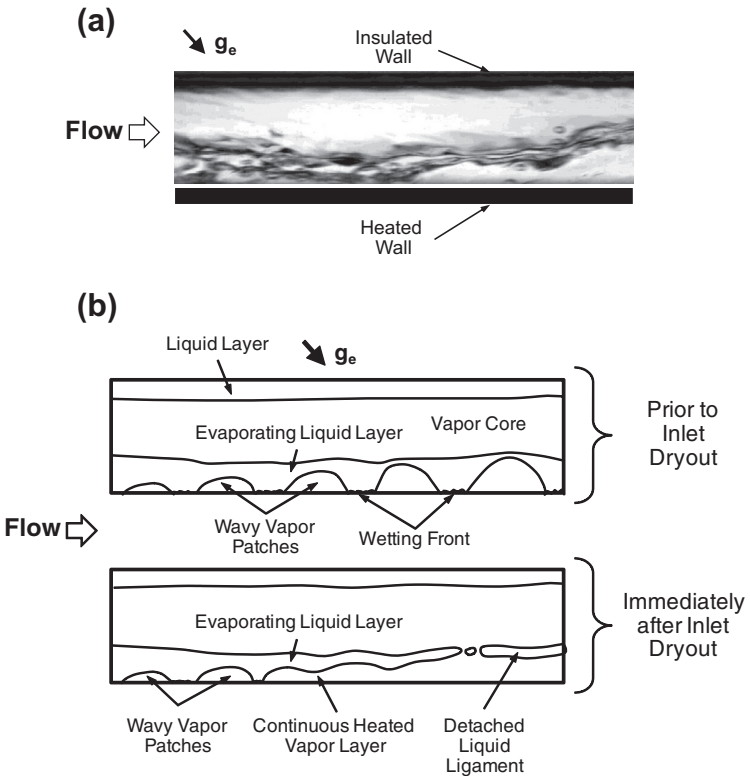

Fig. 9. (a) Photo of the flow in the inlet region for $G/\rho_f = 0.224$ m/s, $x_{e,in} = 0.01$ and $\theta = 315°$ immediately after inlet dryout. (b) Idealized representation of the flow prior to, and immediately after the inlet dryout.

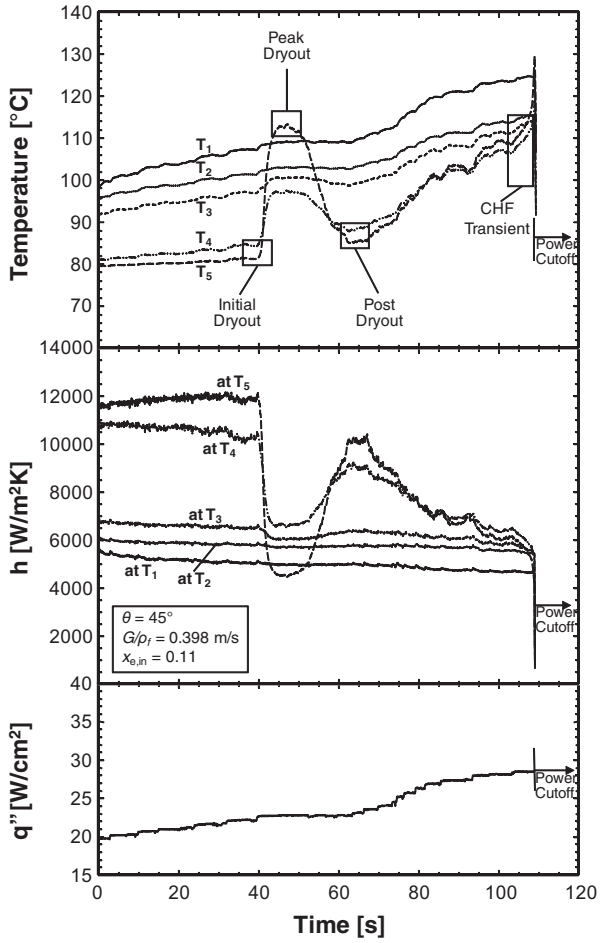

Fig. 10. Temporal records of wall temperatures, heat transfer coefficients and input wall heat flux for $G/\rho_f = 0.398$ m/s, $x_{e,in} = 0.11$ and $\theta = 45°$.

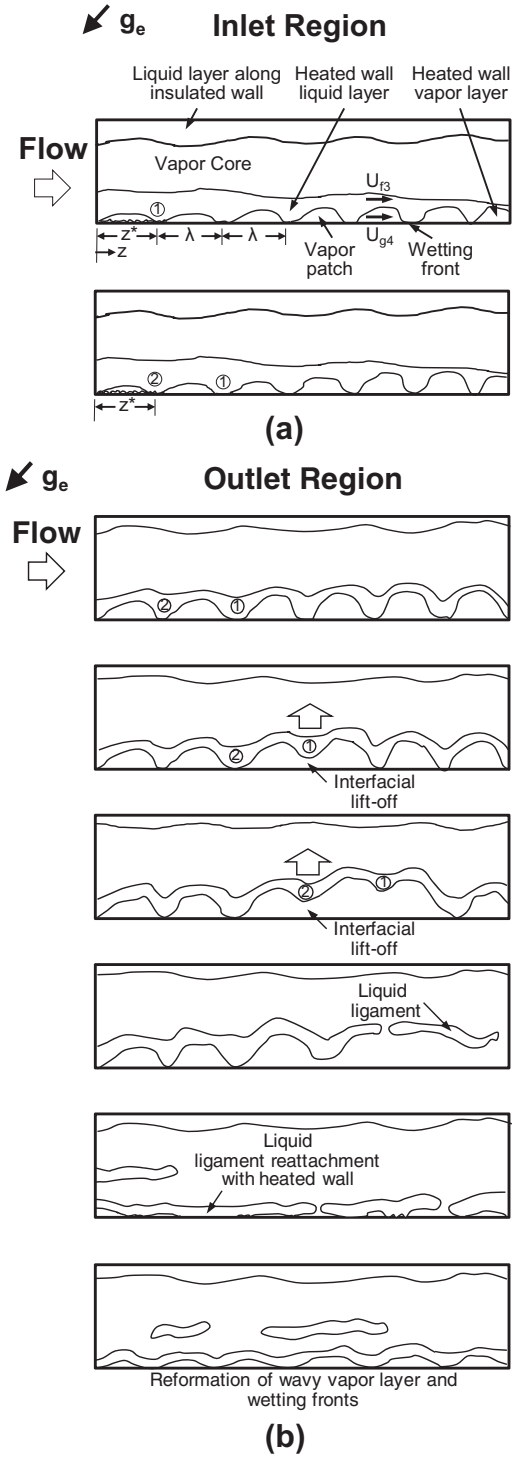

Fig. 11. Illustration of flow behavior during the dryout episode for $G/\rho_f = 0.398$ m/s, $x_{e,in} = 0.11$ and $\theta = 45°$ in the (a) inlet region and (b) outlet region.

Fig. 9(a) shows a representative photo of interfacial behavior immediately after the temperature spike at T_1. Fig. 9(b) shows corresponding idealized representations of interfacial behavior based on observations from multiple video images. Before dryout, intense boiling initiates a series of vapor patches mimicking a wavy vapor layer 4 beneath liquid layer 3 adjacent to the heated wall. Cooling of the wall is still possible through wetting fronts between the vapor patches. Increasing the wall heat flux causes separation – lift-off – of the liquid–vapor interface in the wetting fronts, resulting in a continuous vapor layer. This explains the temperature spike at T_1 and corresponding sharp decrease in the heat transfer coefficient upstream. The interfacial lift-off is also responsible for formation of elongated liquid ligaments – remnants of the near-heated-wall liquid layer – that are carried downstream. Restoration of steady conditions at T_1 following the spike can be explained by reattachment of the liquid ligaments with the heated wall downstream. This rewetting effect causes re-initiation of wetting fronts downstream. Favorable cooling conditions at these downstream wetting fronts cause heat from the upstream vapor-insulated region to be conducted axially through the wall to the middle and outlet regions. This behavior provides support for the need to have adequate wall thickness to support lateral heat conduction and avoid pre-mature CHF detection. Another reason for the downstream heat transfer enhancement is the increase in velocities of all the flow layers because of evaporation.

Fig. 10 shows a composite plot of temporal records for $G/\rho_f = 0.398$ m/s, $x_{e,in} = 0.11$ and $\theta = 45°$. In this case, momentary dryout is encountered in the outlet region of the heated wall and detected by thermocouples T_4 and T_5. The dryout is initiated at 40 s, with T_5 indicating significantly higher temperatures than T_4. The spike reaches peak temperature – peak dryout – around 47 s before subsiding back to post-dryout steady-state at 63 s. Notice that the electrical power input is held constant during the entire dryout episode. Between the initial and peak dryout, the local heat transfer coefficient at T_5 drops from 12,000 to 4500 W/m^{2}K in 5 s, then rises sharply between peak and post dryout to a value about 20% below where it started. Increasing electrical power input in small

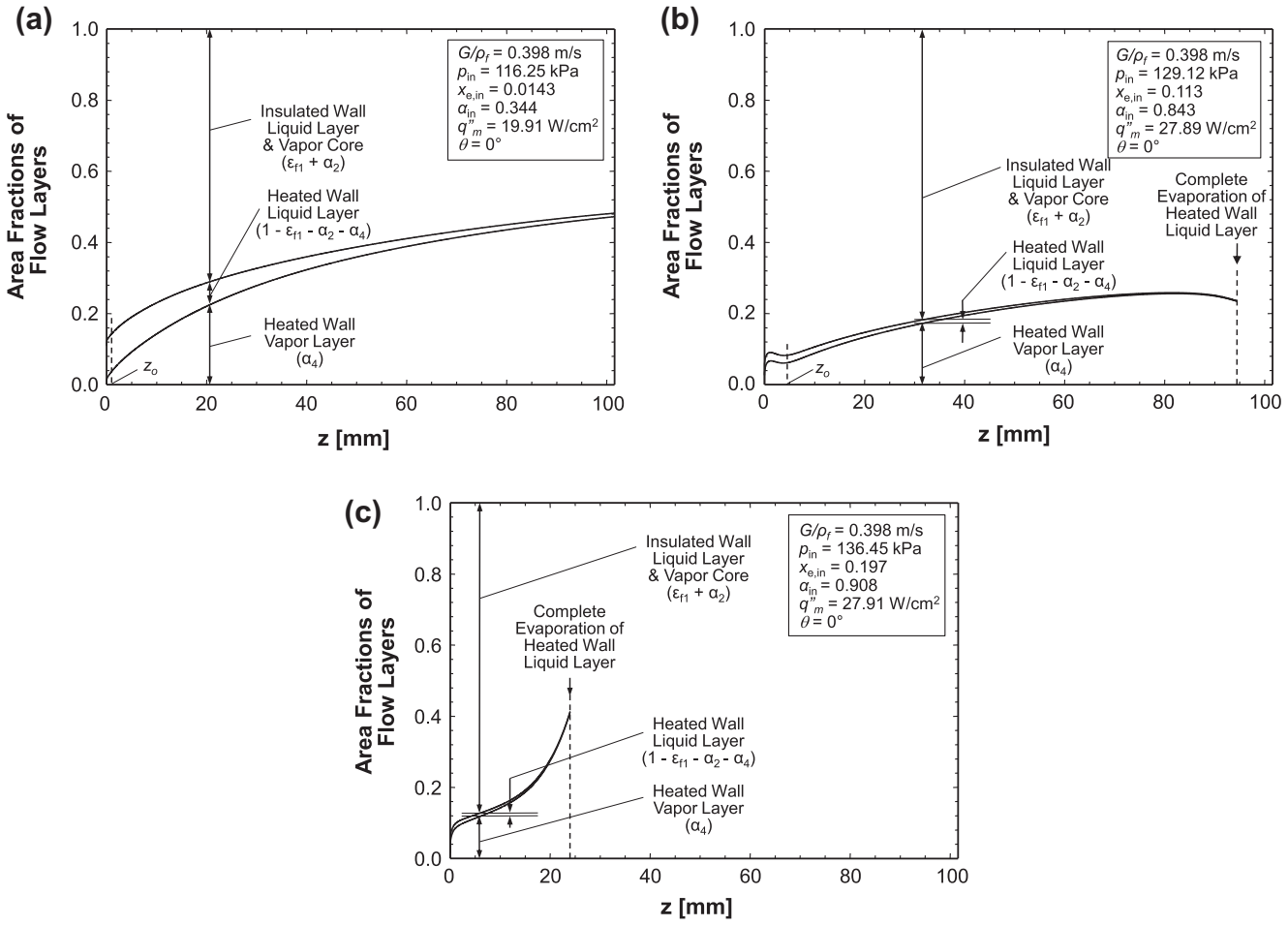

Fig. 12. Separated four-layer model predictions of area fractions for G/ρ_f = 0.398 m/s, θ = 0° and (a) $x_{e,in}$ = 0.0143, (b) $x_{e,in}$ = 0.113, and (c) $x_{e,in}$ = 0.197.

increments after the dryout episode causes incremental rise in T_4 and T_5, and corresponding monotonic decreases in the heat transfer coefficients at T_4 and T_5 until CHF is ultimately detected in the outlet region. Notice that the local heat transfer coefficients in the inlet region display far lesser dependence on the wall heat flux than at T_4 and T_5. It is interesting to note that incorrectly identifying the dryout episode as CHF would result in a CHF value of 22.9 W/cm^2 instead of the true value of 28.5 W/cm^2.

Fig. 11(a) shows schematic representations of the interfacial behavior observed in the inlet region for G/ρ_f = 0.398 m/s, $x_{e,in}$ = 0.11 and θ = 45°. The characteristic wavy vapor layer regime is observed throughout the inlet region. Wetting fronts are established consistently at the same axial distance, z^*, from the leading edge of the heated wall. The schematics show a wetting front, labeled 1, forming upstream and propagating along the heated wall as a second wetting front 2 is formed at z^*. The wetting fronts are formed between vapor patches mimicking a wavy vapor layer with uniform wavelength λ.

Fig. 11(b) shows schematics of the flow behavior in the outlet region during the temporary dryout episode captured in Fig. 10. Notice that the liquid layer adjacent to the heated wall suffers appreciable thinning due to both evaporation and increased shear stresses resulting from axial acceleration of the flow layers. The dryout episode is initiated with wetting front 1 lifting from the heated wall, causing the vapor patches upstream and downstream of 1 to merge into a single longer vapor patch. With a larger portion of the heated wall now insulated, more heat is concentrated in wetting front 2, causing lifting of 2 as well. This action causes the liquid layer to shatter into liquid ligaments that are entrained in the vapor core. The temporary dryout is terminated when the vapor core shear forces cause liquid ligaments to reattach with the heated wall, restoring the wavy vapor layer and wetting front formations. CHF is achieved at a later time when these newly established wetting fronts begin to lift from the heated wall.

5. Separated model predictions

Using the separated four-layer model summarized in Table 1, the thicknesses and velocities of the various layers comprising the flow are computed for three sets of operating conditions to provide further insight into the dryout phenomena discussed thus far.

Fig. 12(a)–(c) show variations of computed area fractions of the four layers along the heated portion of the flow channel at CHF- for G/ρ_f = 0.398 m/s, θ = 0° and different inlet qualities. The area fractions are segregated by $(\varepsilon_{f1} + \alpha_2)$ for the combined insulated wall liquid layer and vapor core, $(1 - \varepsilon_{f1} - \alpha_2 - \alpha_4)$ for the heated wall liquid layer, and α_4 for the heated wall wavy vapor layer.

For $x_{e,in}$ = 0.0143 and α_{in} = 0.344, Fig. 12(a) shows the heated wall vapor layer's mean thickness increases in the axial direction because of evaporation. This causes the thickness of heated liquid layer to decrease monotonically, creating greater susceptibility to breakup into ligaments downstream. The model also shows the flow areas of the insulated wall liquid layer and vapor core decreasing axially due to the increasing shear stresses.

For higher inlet qualities of $x_{e,in}$ = 0.113 and α_{in} = 0.843, Fig. 12(b) shows the combined insulated wall liquid layer and vapor core area fraction, $(\varepsilon_{f1} + \alpha_2)$, occupies the majority of the channel's cross-sectional area. The heated wall liquid layer is much

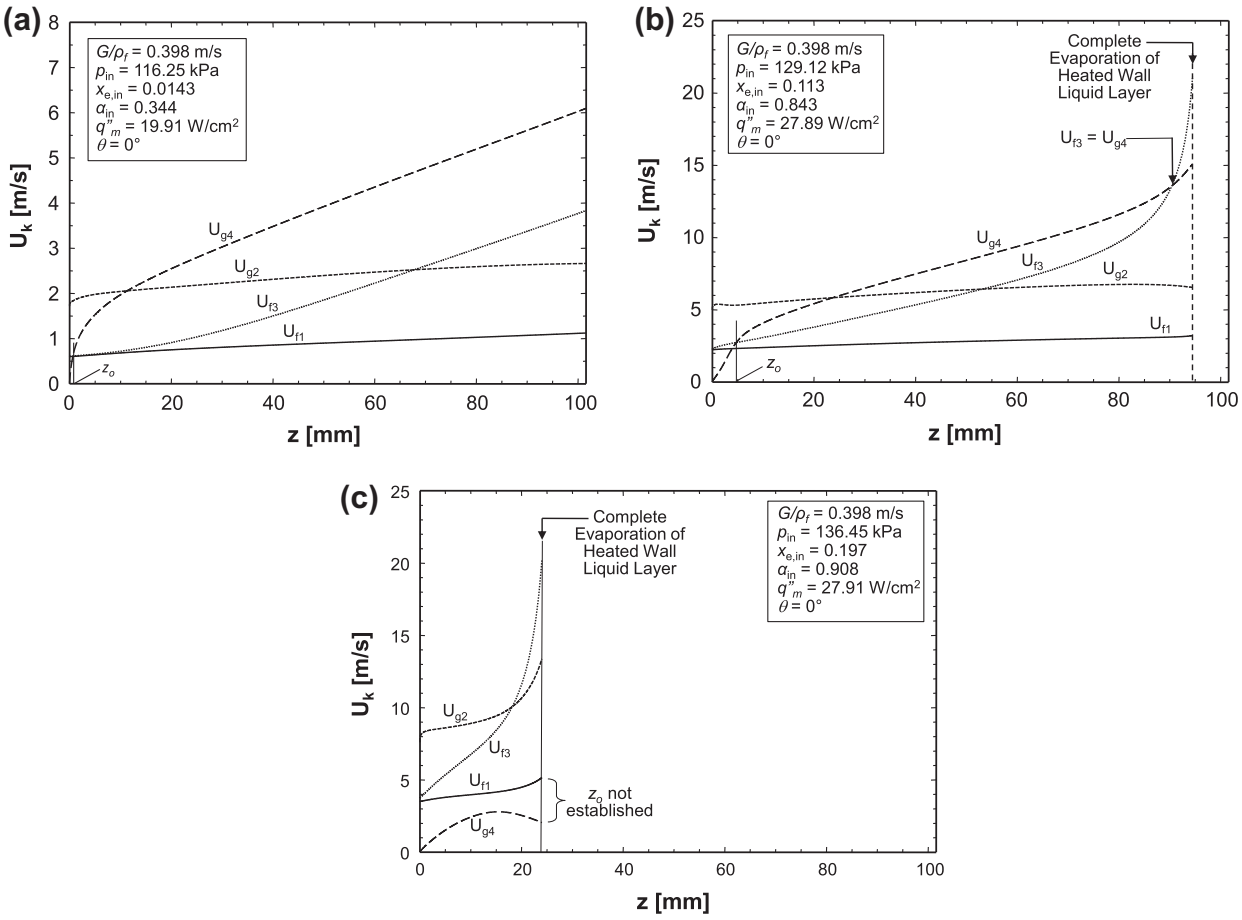

Fig. 13. Separated four-layer model predictions of layer velocities for $G/\rho_f = 0.398$ m/s, $\theta = 0°$ and (a) $x_{e,in} = 0.0143$, (b) $x_{e,in} = 0.113$, and (c) $x_{e,in} = 0.197$.

thinner compared to $x_{e,in} = 0.0143$, Fig. 12(a), and is completely evaporated at $z = 94$ mm, before the end of the heated wall. For the highest inlet qualities of $x_{e,in} = 0.197$ and $\alpha_{in} = 0.908$, Fig. 12(c) shows further thinning of the heated wall liquid layer and complete evaporation even further upstream, at 24 mm. The predicted thinning and complete evaporation of the heated wall liquid layer may help explain the aforementioned tendency of this layer to break apart into liquid ligaments and cause temporary pre-CHF dryout.

Fig. 13(a)–(c) shows variations of computed phase velocities of the four layers along the heated portion of the flow channel at CHF- for $G/\rho_f = 0.398$ m/s and $\theta = 0°$ at different inlet qualities. Due to the fluid entering the heated portion of the channel with a finite vapor void, the two-phase mixture enters the heated channel region with velocities of the liquid film sheathing the four channel walls, U_{f1}, and vapor core, U_{g2}, that are greater than G/ρ_f. Shown in Fig. 13(a) for $x_{e,in} = 0.0143$ and $\alpha_{in} = 0.344$, the vapor core velocity is significantly higher than that of the liquid layer along the insulated and heated walls. The velocities of the insulated walls' liquid layer, U_{f1}, and vapor core, U_{g2}, show comparatively minor variations along the heated portion of the channel. However, the velocity of heated wall wavy vapor layer, U_{g4}, increases drastically from the leading edge of the heated wall due to evaporation of the heated wall liquid layer 3. The velocity of the heated wall liquid layer, U_{f3}, also increases sharply, mostly because of the increasing shear stresses. Location z_o in Fig. 13(a) indicates where U_{g4} just surpasses U_{f3}.

Fig. 13(b) shows velocity predictions for the different layers for higher inlet quality of $x_{e,in} = 0.113$ and $\alpha_{in} = 0.843$. The increased inlet vapor void produces very high inlet velocities for the vapor core, U_{g2}, and insulated walls' liquid layer, U_{f1}. However, U_{g2} and U_{f1} show little variation along the heated portion of the channel. Strong axial velocity increases are predicted for the heated wall liquid layer, U_{f3}, and heated wall wavy vapor layer, U_{g4}. Two interesting observations are (i) U_{f3} surpassing U_{g4} and (ii) full evaporation of the heated wall liquid layer 3 downstream.

Fig. 13(c) shows velocity predictions for $x_{e,in} = 0.197$ and $\alpha_{in} = 0.908$. Here, the velocity of the heated wall wavy vapor layer, U_{g4}, never surpasses that of the heated liquid layer, U_{f3}. Additionally, U_{f3} is shown exceeding U_{g4}, and the heated wall liquid layer fully evaporated over a small fraction of the heated length.

These predictions of area ratios and velocities for the different flow layers provide valuable insight into the pre-CHF anomalies. First, they identify the thinning and eventual evaporation of the heated wall liquid layer as the primary cause for these occurrences. They also point to lateral conduction along the heated wall as essential to channeling heat from momentary dry regions to adequately cooled regions, especially during the pre-CHF dryout episodes. This in turn points to the need to use an adequately thick and thermally conducting heated wall to obtain reliable CHF data. It is recommended that future CHF studies adopt the minimum heated wall thickness criterion discussed earlier to help ensure consistency between CHF databases.

6. Conclusions

This study investigated the interfacial phenomena preceding the occurrence of CHF for flow boiling with a finite inlet vapor void. Experiments were conducted in a rectangular channel that is heated along one side using FC-72 as working fluid. Temporal records of the heated wall temperatures were used to track the

complex transient response of the heated wall, and identify differences between temperature excursions associated with momentary localized dryout and those with true CHF. Key findings from the study are as follows.

(1) The flow enters the channel fully separated, with a liquid layer sheathing all four channel walls surrounding a central vapor core. At high heat fluxes, a wavy vapor layer begins to form beneath the heated wall liquid layer, and cooling is available mostly through wetting fronts in accordance with the Interfacial Lift-off Model. However, certain operating conditions cause monetary dryout well below true CHF.
(2) Localized dryout is observed prior to CHF for upward-facing heated wall orientations ($\theta = 315°$, 0° and 45°) in the inlet region of the heated wall for low inlet mass velocities ($G/\rho_f \leqslant 0.315$ m/s), and the outlet region for mid-range velocities ($0.542 \geqslant G/\rho_f \geqslant 0.315$ m/s). This phenomenon is associated with breakup of the heated wall liquid layer into ligaments that are entrained in the vapor core. The wall is able to recover from this dryout by a combination of reattachment of ligaments with the heated wall and heat conduction.
(3) Breakup into ligaments is the result of axial thinning of the heated wall liquid layer caused by both evaporation and axially increasing shear stresses. The separated flow model is an effective tool for describing this thinning effect and eventual evaporation of the heated wall liquid layer.
(4) Experimental studies must adopt minimum heated wall thickness criteria and consistent temperature detection methods to achieve reliable CHF data.

Acknowledgment

The authors are grateful for the support of this project by the National Aeronautics and Space Administration (NASA) under Grant no. NNX13AC83G.

References

[1] F.P. Chiaramonte, J.A. Joshi, Workshop on critical issues in microgravity fluids, transport, and reaction processes in advanced human support technology – final report, NASA TM-2004-212940, 2004.
[2] The National Academies, Recapturing a Future for Space Exploration: Life and Physical Sciences Research for a New Era, National Academies Press, Washington, DC, 2011.
[3] T.M. Anderson, I. Mudawar, Microelectronic cooling by enhanced pool boiling of a dielectric fluorocarbon liquid, J. Heat Transfer – Trans. ASME 111 (1989) 752–759.
[4] I. Mudawar, A.H. Howard, C.O. Gersey, An analytical model for near-saturated pool boiling CHF on vertical surfaces, Int. J. Heat Mass Transfer 40 (1997) 2327–2339.
[5] R.A. DeBortoli, S.J. Green, B.W. LeTourneau, M. Troy, A. Weiss, Forced-Convection Heat Transfer Burn-Out Studies for Water in Rectangular and Round Tubes at Pressures Above 500 psia, WAPD-188, Westinghouse Electric Corp, Pittsburgh, PA, 1958.
[6] T.C. Willingham, I. Mudawar, Forced-convection boiling and critical heat flux from a linear array of discrete heat sources, Int. J. Heat Mass Transfer 35 (1992) 2879–2890.
[7] T.N. Tran, M.W. Wambsganss, D.M. France, Small circular- and rectangular-channel boiling with two refrigerants, Int. J. Multiphase Flow 22 (1996) 485–498.
[8] M. Monde, T. Inoue, Critical heat flux in saturated forced convective boiling on a heated disk with multiple impinging jets, J. Heat Transfer – Trans. ASME 113 (1991) 722–727.
[9] Y. Katto, M. Kunihiro, Study of the mechanism of burn-out in boiling system of high burn-out heat flux, Bull. JSME 16 (1973) 1357–1366.
[10] D.C. Wadsworth, I. Mudawar, Enhancement of single-phase heat transfer and critical heat flux from an ultra-high-flux-source to a rectangular impinging jet of dielectric liquid, J. Heat Transfer – Trans. ASME 114 (1992) 764–768.
[11] M.E. Johns, I. Mudawar, An ultra-high power two-phase jet-impingement avionic clamshell module, J. Electron. Packag. – Trans. ASME 118 (1996) 264–270.
[12] L. Lin, R. Ponnappan, Heat transfer characteristics of spray cooling in a closed loop, Int. J. Heat Mass Transfer 46 (2003) 3737–3746.
[13] M. Visaria, I. Mudawar, Theoretical and experimental study of the effects of spray orientation on two-phase spray cooling and critical heat flux, Int. J. Heat Mass Transfer 51 (2008) 2398–2410.
[14] R.L. Webb, The evolution of enhanced surface geometries for nucleate boiling, Heat Transfer Eng. 2 (1981) 46–69.
[15] P.J. Marto, V.J. Lepere, Pool boiling heat transfer from enhanced surfaces to dielectric fluids, J. Heat Transfer – Trans. ASME 104 (1982) 292–299.
[16] V. Khanikar, I. Mudawar, T. Fisher, Effects of carbon nanotube coating on flow boiling in a micro-channel, Int. J. Heat Mass Transfer 52 (2009) 3805–3817.
[17] M.K. Sung, I. Mudawar, Experimental and numerical investigation of single-phase heat transfer using a hybrid jet-impingement/micro-channel cooling scheme, Int. J. Heat Mass Transfer 49 (2006) 682–694.
[18] M.K. Sung, I. Mudawar, Correlation of critical heat flux in hybrid jet impingement/micro-channel cooling scheme, Int. J. Heat Mass Transfer 49 (2006) 2663–2672.
[19] I. Mudawar, Recent advances in high-flux, two-phase thermal management, J. Therm. Sci. Eng. Appl. 5(2), 2013, pp. 1-15.
[20] N. Zuber, M., Tribus, J.W. Westwater, The hydrodynamic crisis in pool boiling of saturated and subcooled liquids, in: Int. Dev. Heat Transfer: Proc. 1961–62 Int. Heat Transfer Conf., Boulder, CO, 1961, pp. 230–236.
[21] D.D. Hall, I. Mudawar, Critical heat flux (CHF) for water flow in tubes. I. Compilation and assessment of world CHF data, Int. J. Heat Mass Transfer 43 (2000) 2573–2604.
[22] S.S. Kutateladze, A.I. Leont'ev, Some applications of the asymptotic theory of the turbulent boundary layer, in: Proc. third Int. Heat Transfer Conf., Chicago, Illinois, vol. 3, 1966, pp. 1–6.
[23] L.S. Tong, Boundary-layer analysis of the flow boiling crisis, Int. J. Heat Mass Transfer 11 (1968) 1208–1211.
[24] W. Hebel, W. Detavernier, M. Decreton, A contribution to the hydrodynamics of boiling crisis in a forced flow of water, Nucl. Eng. Des. 64 (1981) 443–445.
[25] J. Weisman, B.S. Pei, Prediction of critical heat flux in flow boiling at low qualities, Int. J. Heat Mass Transfer 26 (1983) 1463–1477.
[26] C.H. Lee, I. Mudawar, A mechanistic critical heat flux model for subcooled flow boiling based on local bulk flow conditions, Int. J. Multiphase Flow 14 (1988) 711–728.
[27] J.E. Galloway, I. Mudawar, CHF mechanism in flow boiling from a short heated wall. Part 1. Examination of near-wall conditions with the aid of photomicrography and high-speed video imaging, Int. J. Heat Mass Transfer 36 (1993) 2511–2526.
[28] J.E. Galloway, I. Mudawar, CHF mechanism in flow boiling from a short heated wall. Part 2. Theoretical CHF model, Int. J. Heat Mass Transfer 36 (1993) 2527–2540.
[29] J.C. Sturgis, I. Mudawar, Critical heat flux in a long, rectangular channel subjected to onesided heating. I. Flow visualization, Int. J. Heat Mass Transfer 42 (1999) 1835–1847.
[30] J.C. Sturgis, I. Mudawar, Critical heat flux in a long, rectangular channel subjected to onesided heating. II. Analysis of critical heat flux data, Int. J. Heat Mass Transfer 42 (1999) 1849–1862.
[31] H. Zhang, I. Mudawar, M.M. Hasan, Flow boiling CHF in microgravity, Int. J. Heat Mass Transfer 48 (2005) 3107–3118.
[32] L. Wojtan, R. Revellin, J.R. Thome, Investigation of saturated critical heat flux in a single uniformly heated microchannel, Exp. Therm. Fluid Sci. 30 (2006) 765–774.
[33] D. Del Col, S. Bortolin, Investigation of dryout during flow boiling in a single microchannel under non-uniform axial heat flux, Int. J. Therm. Sci. 57 (2012) 25–36.
[34] S.M. Kim, I. Mudawar, Universal approach to predicting saturated flow boiling heat transfer in mini/micro-channels. Part I. Dryout incipience quality, Int. J. Heat Mass Transfer **64**, 2013, pp. 1226-1238.
[35] Y. Katto, General features of CHF of forced convection boiling in uniformly heated rectangular channels, Int. J. Heat Mass Transfer 24 (1981) 1413–1419.
[36] C. Martín-Callizo, Flow boiling heat transfer in single vertical channel of small diameter, Ph.D. Thesis, Royal Institute of Technology, Sweden, 2010.
[37] R. Ali, B. Palm, Dryout characteristics during flow boiling of R134a in vertical circular minichannels, Int. J. Heat Mass Transfer 54 (2011) 2434–2445.
[38] W.P. Baek, S.H. Chang, KAIST CHF data, Personal communication, Korea Advanced Institute of Science and Technology, Taejon, South Korea, December 8, 1997.
[39] G.M. Roach Jr, S.I. Abdel-Kahlik, S.M. Ghiaasiaan, M.F. Dowling, S.M. Jeter, Low-flow critical heat flux in heated microchannels, Nucl. Sci. Eng. 131 (1999) 411–425.
[40] K.M. Becker, Burnout measurements in vertical round tubes, effect of diameter, AE-TPM-RL-1260, Aktiebolaget Atomenergi, 1970.
[41] W. Yu, D.M. France, M.W. Wambsganss, J.R. Hull, Two-phase pressure drop, boiling heat transfer, and critical heat flux to water in a small-diameter horizontal tube, Int. J. Multiphase Flow 28 (2002) 927–941.
[42] C.R. Kharangate, I. Mudawar, M.M. Hasan, Experimental and theoretical study of critical heat flux in vertical upflow with inlet vapor void, Int. J. Heat Mass Transfer 55 (2012) 360–374.
[43] G. Guglielmini, E. Nannei, On the effect of heating wall thickness on pool boiling burnout, Int. J. Heat Mass Transfer 19 (1976) 1073–1075.
[44] H.S. Lee, H. Merte, Spherical vapor bubble growth in uniformly superheated liquids, Int. J. Heat Mass Transfer 39 (1996) 2427–2447.

[45] Y. Ma, J.N. Chung, An experimental study of forced convection boiling in microgravity, Int. J. Heat Mass Transfer 41 (1998) 2371–2382.
[46] Y. Ma, J.N. Chung, A study of bubble dynamics in reduced gravity forced-convection boiling, Int. J. Heat Mass Transfer 44 (2001) 399–415.
[47] C.O. Gersey, I. Mudawar, Effects of heater length and orientation on the trigger mechanism for near-saturated flow boiling critical heat flux. I. Photographic study and statistical characterization of the near-wall interfacial features, Int. J. Heat Mass Transfer 38 (1995) 629–641.
[48] C.O. Gersey, I. Mudawar, Effects of heater length and orientation on the trigger mechanism for near-saturated flow boiling critical heat flux. II. Critical heat flux model, Int. J. Heat Mass Transfer 38 (1995) 643–654.
[49] H. Zhang, I. Mudawar, M.M. Hasan, Experimental assessment of the effects of body force, surface tension force, and inertia on flow boiling CHF, Int. J. Heat Mass Transfer 45 (2002) 4079–4095.
[50] H. Zhang, I. Mudawar, M.M. Hasan, A method for assessing the importance of body force on flow boiling CHF, J. Heat Transfer – Trans ASME 126 (2004) 161–168.
[51] C.R. Kharangate, I. Mudawar, M.M. Hasan, Experimental and theoretical study of critical heat flux in vertical upflow with inlet vapor void, Int. J. Heat Mass Transfer 55 (2012) 360–374.
[52] C.R. Kharangate, I. Mudawar, M.M. Hasan, Photographic study and modeling of critical heat flux in horizontal flow boiling with inlet vapor void, Int. J. Heat Mass Transfer 55 (2012) 4154–4168.
[53] C. Konishi, I. Mudawar, M.M. Hasan, Investigation of the influence of orientation on critical heat flux for flow boiling with two-phase inlet, Int. J. Heat Mass Transfer 61 (2013) 176–190.
[54] C. Konishi, I. Mudawar, M.M. Hasan, Criteria for negating the influence of gravity on flow boiling critical heat flux with two-phase inlet conditions, Int. J. Heat Mass Transfer 65 (2013) 203–218.